Catalysis Today 427 (2024) 114404

Contents lists available at ScienceDirect

Catalysis Today

journal homepage: www.elsevier.com/locate/cattod

Direct hydrogenation of CO_2 to aromatics via Fischer-Tropsch route over tandem K-Fe/Al_2O_3+H-ZSM-5 catalysts: Influence of zeolite properties

Raúl Murciano, José M. Serra, Agustín Martínez *

Instituto de Tecnología Química, Universitat Politècnica de València (UPV)-Consejo Superior de Investigaciones Científicas (CSIC), Avenida de los Naranjos s/n, 46022 Valencia, Spain

ARTICLE INFO

Keywords:
CO_2 hydrogenation
Aromatics
BTEX
Tandem catalyst
Fischer-Tropsch
H-ZSM-5 zeolite

ABSTRACT

Direct hydrogenation of CO_2 to valuable aromatics using multifunctional catalysts is an attractive technology to produce low-carbon footprint chemicals. In this work, the relevant zeolite parameters driving the formation of total and BTEX aromatics from CO_2 and H_2 on tandem K-Fe/γ-Al_2O_3+H-ZSM-5 catalysts following the Fischer-Tropsch (FT)-mediated route were investigated. To this end, a set of H-ZSM-5 zeolites covering a wide range of physicochemical properties (density of Brønsted and Lewis acid sites, external acidity, crystallite size, and mesoporosity) was used, characterized by different techniques (ICP-OES, XRD, N_2 physisorption, FTIR-pyridine, FTIR-2,6,-di-tert-butyl pyridine, XPS, ^{27}Al MAS NMR, and electron microscopy), and evaluated in CO_2 hydrogenation at 400 °C, 30 bar, $H_2/CO_2 = 3.1$, and GHSV of 4700 mL/($g_{Fe\text{-}cat}$·h). At these conditions, high and stable CO_2 conversions of 50 – 55% and low CO selectivity of ca. 10% were obtained for the Fe-based and tandem catalysts. The density and, to a certain extent, the strength of Brønsted acid sites were found the main parameters determining the selectivity of aromatics, reaching initial (TOS = 1.5 h) values of about 79% and 40% in liquid (C_{5+}) and total hydrocarbons, respectively, for the catalyst based on the most acidic zeolite. Lewis acid sites associated to extraframework Al species (EFAL), by contrast, did not appear to play a relevant role in our conditions. Moreover, although a positive effect of the total amount and strength of Brønsted acid sites on the selectivity to the most valuable BTEX aromatics was inferred from our results, the external Brønsted acidity was the most influential factor in this case. Hence, a remarkable BTEX selectivity of 75% in aromatics was achieved for the zeolite previously submitted to a surface-passivation treatment by silylation.

1. Introduction

The use or renewable energy to displace fossil energy and the implementation of *Carbon Capture and Utilization* (CCU) technologies are key strategies to achieve the ambitious goal of net-zero carbon emissions required to combat climate crisis. The CCU strategy can bring potential to mitigate carbon emissions by using CO_2 captured from carbon-intensive industries (e.g., cement and steel) or even directly from the air as a carbon feedstock to produce value-added products [1,2]. Among the available CCU options, the thermocatalytic hydrogenation of CO_2 to valuable liquid fuels and chemicals (e.g., methanol, gasoline, jet fuel, aromatics) using green hydrogen is particularly appealing as it additionally provides the possibility to store and easily transport surplus (intermittent) renewable energy in the form of chemical energy. However, most current CCU technologies rely on multi-step processes involving several separation and catalytic processes that result in low overall energy efficiency and high cost. Intensification of the CO_2 hydrogenation process from both the reactor and catalyst design viewpoints might alleviate the above issues laying the ground towards their industrial implementation. An example of this could be the integration of a multifunctional catalyst in an electrochemical ionic membrane reactor (e-CMR) to realize the one-stage conversion of CO_2 and water to valuable hydrocarbons as proposed in the EU-funded eCOCO2 project in which the present study is framed [3].

Aromatic hydrocarbons, particularly the most demanded benzene, toluene, ethylbenzene, and xylenes (BTEX) fraction, are widely used as solvents, fuel additives, and as key building blocks in the production of different types of polymers used in the manufacture of many everyday products. Currently, aromatics are still mostly produced from fossil resources resulting in huge CO_2 emissions. Therefore, the production of sustainable aromatics from captured CO_2 and low-carbon H_2 or from renewable syngas is a promising approach towards climate neutrality.

* Corresponding author.
E-mail address: amart@itq.upv.es (A. Martínez).

https://doi.org/10.1016/j.cattod.2023.114404
Received 24 July 2023; Received in revised form 20 September 2023; Accepted 5 October 2023
Available online 10 October 2023

The direct conversion of CO_2 and H_2 or syngas to aromatic hydrocarbons can proceed through two main catalytic routes depending on the nature of the intermediates involved [4,5]: i) the methanol-mediated route, and ii) the Fischer-Tropsch (FT)-mediated route. In both cases, multifunctional catalysts are required to realize the conversion of CO_2 and H_2 to the intermediate and its subsequent transformation to aromatics via tandem catalysis in a single reactor. Catalysts developed for the methanol-mediated pathway are generally based on the oxide-zeolite concept [6]. In oxide-zeolite systems for CO_2/H_2-to-aromatics conversion, a metal oxide (e.g., $ZnZrO_x$, $ZnCrO_x$, $ZnAlO_x$, $ZnCrO_x$, etc.) containing surface oxygen vacancies, serving as active sites for methanol formation, is integrated with an H-ZSM-5 zeolite that catalyses the conversion of methanol to aromatics via acid catalysis according to the well-known methanol-to-aromatics (MTA) process [7]. On the other hand, most common catalysts for the FT-mediated route combine an iron-based catalyst, active for both the RWGS reaction leading to CO and its subsequent hydrogenation to mainly olefins through FT chemistry, with an H-ZSM-5 zeolite that produce aromatics from the olefin intermediates. The mechanism by which olefins are converted to aromatics on H-ZSM-5 still remains debated and both the hydrogen-transfer [8] and dehydroaromatization [9] pathways have been proposed in the literature.

A characteristic feature of the bifunctional oxide-zeolite systems is the possibility to achieve outstanding selectivities to specific hydrocarbons (e.g., aromatics) thanks to the fact that the conversion of the methanol intermediate occurs under the shape-selective environment provided by the microporous zeolite environment. For instance, Ni et al. reported a high selectivity of aromatics of ca. 74% in the hydrocarbons fraction at CO_2 conversion of around 7% over a $ZnAlO_x$+H-ZSM-5 catalyst [10]. However, these catalysts present two major drawbacks: the conversion of CO_2 is relatively low (generally below 20%) and the selectivity of CO is undesirably high, typically above 50% [10–12]. Thus, achieving higher CO_2 conversion while keeping low selectivity of CO (and CH_4) are important current challenges in the development of efficient oxide-zeolite systems. In contrast, although less selective, tandem Fe-based+H-ZSM-5 catalysts operating through the FT-mediated route can achieve much higher CO_2 conversions ($> 40\%$) along with reduced CO selectivity ($< 20\%$) at equivalent reaction conditions [13–15].

As discussed above, thanks to its unique pore topology, H-ZSM-5 is the zeolite of choice in both oxide-zeolite and Fe-based+zeolite multifunctional catalysts to directly produce aromatics from CO_2/H_2 or syngas through, respectively, the methanol- and FT-mediated pathways. Therefore, fine tuning of the zeolite properties becomes essential to maximize the total selectivity of aromatics, and especially to the most demanded BTEX fraction. Thus, efforts were devoted in previous studies to improve the aromatization performance of H-ZSM-5 in tandem or composite catalysts by tailoring the zeolite acidity, for instance by modifying the Si/Al ratio [14] or by introducing metals such as Ni [16] and P [17] to regulate the acid strength. The incorporation of Ga and Zn species in H-ZSM-5 was also applied to enhance the aromatics formation by promoting dehydrogenation reactions on the metal-related Lewis acid sites [18,19]. Furthermore, passivation of the external acid sites by deposition of an external SiO_2 layer through silylation treatments [20–22] or by constructing more sophisticated core-shell structures (e.g. H-ZSM-5@Silicalite-1) [7,13,23] proved to be an effective strategy to improve the selectivity of the most valuable BTEX (and para-xylene) aromatics. Besides acidity, the morphology and size of the zeolite crystallites were also relevant properties affecting the aromatization performance of H-ZSM-5 [24–26].

From the process viewpoint, the operating temperature is an important parameter to maximize aromatics selectivity as it should effectively couple the reactions occurring on the two functionalities of the tandem catalysts, that is, the CO_2 reduction to intermediates on the oxide or Fe-based component, depending on the catalytic route, and the aromatization of the intermediates on the zeolite, without excessively promoting side reactions leading to unwanted products like CO (from CO_2/H_2) or CO_2 (from syngas), CH_4, and saturated hydrocarbons. In the particular case of CO_2 hydrogenation, reaction temperatures in the range of 300 – 350 °C are applied in most of the earlier works. However, in the context of the eCOCO2 project framing this study, a minimum reaction temperature of 400 °C has to be employed to ensure an efficient integration of the catalyst in the electrochemical membrane reactor. Considering this constraint and its potential influence on catalyst performance, the present work aims at elucidating the most relevant zeolite parameters driving the formation of total and BTEX aromatics via hydrogenation of CO_2 over tandem Fe-based+H-ZSM-5 catalysts at the relatively high reaction temperatures (specifically at 400 °C) compatible with the e-CMR operation.

2. Experimental

2.1. Preparation of catalysts

2.1.1. CO_2 reduction function: K-Fe/γ-Al_2O_3 catalyst

The CO_2 reduction function operating through the Fischer-Tropsch route consisted of a potassium-promoted iron catalyst supported on a high-purity commercial γ-Al_2O_3 (Puralox TH 100/150, Sasol Materials). The K-Fe/γ-Al_2O_3 catalyst was prepared by incipient wetness co-impregnation of the pre-dried alumina carrier with an aqueous solution containing the amounts of $Fe(NO_3)_3{\cdot}9\ H_2O$ (Merck, ≥ 98%) and KNO_3 (Merck, 99%) precursors required to achieve an iron loading of 20 wt% and an K/Fe atomic ratio of 1 (nominal values). After impregnation, the solid was dried at 110 °C overnight and subsequently calcined in air flow at 500 °C for 6 h using a heating rate of 1 °C/min.

2.1.2. Acid function: H-ZSM-5 zeolites

The medium-pore H-ZSM-5 zeolite was used as acid function of the multifunctional catalysts to produce the aromatic hydrocarbons. A set of eight commercial and home-prepared H-ZSM-5 samples with varying physicochemical properties was employed to derive proper structure-performance correlations. The commercial samples, supplied in the NH_4^+-form, comprised the following zeolites (the bulk Si/Al atomic ratio determined by ICP-OES is given in parenthesis): TZP302A (10) from Tricat, and CBV3023E (16), CBV5020 (22), CBV8020 (31), and CBV28014 (112) from Zeolyst International. The corresponding protonic (H^+) forms were obtained by calcination in a muffle oven under air atmosphere at 500 °C for 3 h (heating rate of 2 °C/min). The produced H-ZSM-5 samples were denoted in this work as MFI-c(x), where "c" refers to their commercial origin when applied and "x" to the bulk Si/Al atomic ratio from ICP-OES analyses.

The commercial MFI-c(31) sample was submitted to a surface-silylation treatment by the chemical liquid deposition (CLD) method using tetraethoxysilane (TEOS, Sigma-Aldrich, ≥ 99%) as silica source in order to passivate the external acid sites. This method has been widely employed to this purpose due to its effectiveness, simplicity, and easy application at larger scales [27–29]. Briefly, 6 g of MFI-c(31) were suspended in 150 mL of *n*-hexane and the mixture refluxed at 60 °C for 30 min under stirring. Then, 0.9 mL of TEOS (corresponding to 4 wt% of SiO_2 loading) was added to the mixture and maintained under stirring and reflux for 1 h. Subsequently, the *n*-hexane solvent was removed by evaporation, the solid was dried at 100 °C overnight and finally calcined under flowing air at 500 °C for 4 h with a ramp of 1 °C/min. The above procedure was repeated 3 times to produce the sample named as MFI-sil (34).

On the other hand, the commercial MFI-c(22) sample was subjected to a desilication treatment under basic conditions to generate intracrystal mesopores via controlled extraction of framework silicon species. To this end, an aqueous solution of 0.2 M NaOH (Scharlab, 98%) and TBAOH (Alfa Aesar, 40 wt% aq. solution) in a TBAOH/(NaOH+TBAOH) molar ratio of 0.4 was mixed with the MFI-c(22) zeolite in a liquid/solid ratio of 25 mL/g and heated under agitation at 80 °C for 1 h. The

resulting material was submitted to repeated washing-centrifugation cycles until the washing waters reached neutral pH, and subsequently dried at 100 °C overnight. The sample was then treated with a 2.5 M NH_4NO_3 aq. solution (liquid/solid ratio = 10 mL/g) at 80 °C for 2 h under reflux in order to replace the Na^+ cations by NH_4^+, separated by centrifugation until neutral pH, and dried in an oven at 100 °C overnight. Next, the NH_4^+-exchanged sample was treated with an 0.2 M aq. solution of oxalic acid at 60 °C for 2 h under reflux (liquid/solid ratio = 10 mL/g) to selectively dealuminate the external zeolite surface [30], washed with deionized water by repeated centrifugations until pH = 7, and eventually calcined under flowing air at 550 °C for 4 h using a heating rate of 2 °C/min. This sample was labelled as MFI-meso(22).

Finally, a nanocrystalline H-ZSM-5 sample was hydrothermally synthesized using as reagents tetraethoxysilane (TEOS, Sigma-Aldrich, ≥ 99%), aluminium isopropoxide (AIP, Sigma-Aldrich, ≥ 98%), and tetrapropylammonium hydroxide (TPAOH, 40 wt% aqueous solution) from a clear gel solution with the following molar composition: 1TEOS:0.01AIP:0.25TPAOH:20 H_2O. The solution was vigorously stirred at room temperature to hydrolyze the TEOS and to eliminate water until a H_2O/SiO_2 molar ratio of 5 was obtained. The resulting solution was introduced in Teflon-lined stainless steel autoclaves, aged in static at 80 °C for 20 h, and then hydrothermally treated at 180 °C for 90 min under rotation. The solid was recovered by centrifugation, washed, dried at 100 °C, and finally calcined in air at 550 °C for 3 h to obtain the sample named here as MFI-nano(46).

2.1.3. Multifunctional K-Fe/γ-Al_2O_3+H-ZSM-5 catalysts

To prepare the multifunctional catalysts, the individual K-Fe/γ-Al_2O_3 and H-ZSM-5 components were first pelletized to granules sizing 0.2 – 0.4 mm and then physically mixed in a 1:1 mass ratio. The mixture was divided into three equivalent parts and loaded to the reactor consecutively to ensure a homogeneous distribution of granules of each component along the catalytic bed.

2.2. Characterization methods

The chemical composition of the samples was determined by inductively coupled plasma-optical emission spectrometry (ICP-OES) in a Varian 715-ES apparatus after dissolution of the solids in an acid mixture of HNO_3:HF:HCl (1:1:3 vol ratio).

Crystalline phases in the materials were identified by powder X-ray diffraction (XRD) in a Panalytical Cubix Pro diffractometer equipped with a graphite monochromator operating at 40 kV and 45 mA using nickel-filtered CuK_α radiation (λ = 0.1542 nm).

Textural properties of the samples were derived from the corresponding N_2 adsorption isotherms recorded at -196 °C on an ASAP-2000 (Micromeritics) equipment after pretreatment at 400 °C and vacuum overnight. Specific surface areas were obtained by the BET method, pore size distributions were derived from the adsorption branch of isotherms by using the Barrett-Joyner-Halenda (BJH) model, and the micropore volume of the H-ZSM-5 zeolites was determined by the *t*-plot method.

Coordination of Al species in the zeolites was assessed by ^{27}Al MAS NMR spectroscopy on fully hydrated samples. The spectra were recorded at room temperature in a Bruker AV-400 WB spectrometer operating at 104.2 MHz and equipped with a 4 mm Bruker BL4mm probe. Samples were packed into zirconia rotors and spun at the magic angle spinning (MAS) at 10 kHz. The ^{27}Al spectra were acquired with pulses of 0.5 μs corresponding to a flip angle of π/18 and chemical shifts were referred to a 0.1 M aqueous solution of $Al(NO_3)_3$.

The acidity of zeolites was measured by FTIR spectroscopy of adsorbed pyridine (FTIR-Py). FTIR-Py spectra were recorded in a Nicolet 710 FTIR apparatus on self-supported wafers (10 mg/cm^2) previously pretreated at 400 °C overnight under dynamic vacuum of 10^{-4} Pa. Afterwards, $1.8{\cdot}10^3$ Pa of pyridine were admitted to the IR cell at room temperature and after equilibration the samples were degassed for 1 h at 250, 350, and 400 °C. After each desorption step, the spectrum was recorded at room temperature and the background subtracted. The amounts of Brønsted and Lewis acid sites were determined from the integrated areas of the bands at ca. 1545 and 1450 cm^{-1}, respectively, using the extinction coefficients reported by Emeis [31].

Additionally, FTIR spectroscopy of adsorbed 2,6-di-*tert*-butyl pyridine (FTIR-DTBPy), a bulky probe molecule unable to penetrate the 10-ring pores of H-ZSM-5, was employed to qualitatively assess the external Brønsted acidity in selected zeolites [32,33]. FTIR-DTBPy spectra were acquired in a Nicolet 710 FTIR instrument using self-supported wafers of ca. 10 mg/cm^2. Prior to the measurements, the zeolites were dehydrated at 400 °C for 12 h and dynamic vacuum of 10^{-2} Pa. Then, the samples were saturated with 2,6-DTBPy at 150 °C for 12 min, evacuated at this temperature for 1 h to remove physisorbed probe molecules, and the spectrum recorded at room temperature.

The Si/Al ratio in the near-surface region (X-ray penetration depth of 6 – 10 nm) of zeolites was analyzed by XPS in a SPECS spectrometer equipped with a 150-MCD-9 detector using a non-monochromatic AlK_α (1486.6 eV) X-ray source. Spectra were recorded using an analyzer pass energy of 30 V, an X-ray power of 200 W, and under an operating pressure of 10^{-9} mbar. Treatment of the spectral signals was performed using the CASA software.

The approximate size and morphology of crystallites in selected zeolites were analyzed by high-resolution field emission scanning transmission microscopy (HRFESEM) or FESEM using, respectively, Zeiss GeminiSEM 500 and Zeiss Ultra-55 electron microscopes. The samples were dispersed on a double-sided carbon adhesive tape attached to the specimen holder without any coating.

Characterization by transmission electron microscopy (TEM) was carried out using a JEOL JEM 1400 Flash microscope operating at 120 kV. Prior to observation by TEM, the samples were suspended in ethanol and submitted to ultrasonication for one minute. Next, the suspension was slowly decanted for two minutes and a drop was extracted from the top side and placed on a holly carbon-coated copper grid.

2.3. CO_2 hydrogenation experiments

The CO_2 hydrogenation tests were performed in a continuous down-flow stainless steel fixed bed reactor (ID 1.3 cm) using a feed gas mixture with molar composition of 22%CO_2/68%H_2/10%Ar (H_2/CO_2 molar ratio = 3.1, Ar used as internal standard for GC analyses). The catalytic experiments, typically lasting 8 – 9 h, were conducted at 400 °C, 30 bar, and space velocity (GHSV), referred to the mass of iron catalyst, of 4700 $mL_{CO2+H2}/(g_{Fe\text{-}cat}{\cdot}h)$. The relatively high reaction temperature used in this study was imposed by the minimum temperature required for the operation of the e-CMR where the catalyst is to be integrated according to the intensification concept proposed in the eCOCO2 project, as explained in the Introduction. Prior to the reaction, the catalysts were in situ reduced in pure H_2 flow at 400 °C for 8 h (ramp of 1 °C/min). The reaction products were periodically analysed by online gas chromatography in a Varian 450 GC equipped with three columns and two detectors: two packed columns (Porapak Q, 13X molecular sieve) connected to a thermal conductivity detector (TCD) for the analysis of CO_2, CO, CH_4, and Ar (reference gas), and a capillary column (TRB-1, 30 m length, 0.25 mm ID, 1 μm thickness) connected to a flame ionization detector (FID) for the analysis of oxygenates and hydrocarbons, as detailed elsewhere [34]. The full product distribution was obtained by combining the TCD and FID chromatograms through the common product methane. Product selectivities are given on a carbon basis unless otherwise stated. Carbon mass balances of 100 ± 2% were obtained for all the reported experiments.

3. Results and Discussion

3.1. Characterization of materials

3.1.1. Properties of K-Fe/γ-Al_2O_3 component

The Fe and K contents of the calcined K-Fe/γ-Al_2O_3 catalyst determined by ICP-OES amounted to 19.8 and 12.7 wt%, respectively, corresponding to an atomic K/Fe ratio of 0.92, in good agreement with the nominal values. The textural properties of the γ-Al_2O_3 carrier and the calcined catalyst measured by N_2 physisorption are shown in Table S1 (Supporting Information). As seen there, the BET area and pore volume decreased from 144 to 38 m^2/g and from 0.61 to 0.20 cm^3/g, respectively, upon impregnation of Fe and K precursors and subsequent calcination. The total pore volume re-calculated per mass of support was 0.35 cm^3/g_{Al2O3} assuming that Fe and K in the calcined sample are present as Fe_2O_3 and K_2O, respectively, which gives an estimated pore blockage of 42% by the supported metal phases.

The crystalline phases present in the calcined and spent catalyst were assessed by XRD. The corresponding XPR patterns are presented in Fig. S1. As observed there, the calcined sample displayed reflections at ca. 46° and 67° (2θ) associated to the γ-Al_2O_3 support (JCPDS 29–0063) and to the K promoter (KNO_3 (rhombohedral): 2θ = 43.1°, JCPDS 03–0482; KNO_3 (orthorhombic): 2θ = 23.6°, 23.8°, 41.1°, JCPDS 5–0377; K_2O: 2θ = 27.7°, 39.3°, JCPDS 23–0493). The presence of KNO_3 phases indicated the incomplete decomposition of the alkali precursor after the calcination step. In addition, α-Fe_2O_3 (2θ = 32.9°, 35.6°, 54.1°, JCPDS 24–0072) was the only crystalline iron phase detected by this technique in the calcined catalyst. On the other hand, Hägg-type iron carbide (χ-Fe_5C_2, 2θ = 33.9°, 35.7°, 37.3°, 39.4°, 40.9°, 41.2°, 42.8°, 43.5°, 44.2°, 45.0°, 50.1°, JCPDS 20–0509) was detected on the reacted catalyst, with no apparent evidences for iron oxide phases. Although iron carbides, and specially χ-Fe_5C_2, have been long considered the active iron phases for the formation of hydrocarbons in the Fischer-Tropsch synthesis (FTS) reaction [35], their highly dynamic behaviour under reaction conditions makes it hard and challenging to establish unambiguous correlations between FTS performance and iron carbide phase [36,37]. Nevertheless, a fair assessment of the active iron phases and their role in the CO_2 hydrogenation reaction over the multifunctional catalysts studied here is beyond the scope of the present work.

3.1.2. Properties of H-ZSM-5 samples

According to XRD, both the commercial and home-prepared zeolites exhibited only the reflections associated to the MFI topology with a high degree of crystallinity (Fig. S2).

The bulk and near-surface Si/Al atomic ratios determined by ICP-OES and XPS, respectively, the mean crystallite sizes, and the textural properties measured by N_2 physisorption of the zeolites are gathered in Table 1. The alike values of bulk and near-surface Si/Al ratios found for the commercial and nanocrystalline zeolites is indicative for an homogeneous composition along their crystallites. Three-cycle silylation of the commercial MFI-c(31) sample lead to an increase in the bulk Si/Al ratio from 31 to 34, which is fully consistent with the expected incorporation of ca. 4 wt% SiO_2 after each silylation cycle. Moreover, in contrast to the starting MFI-c(31) sample, the XPS analysis indicated a Si-enriched surface in the silylated counterpart (near-surface Si/Al = 41 vs. bulk Si/Al = 34) (Table 1) which can be ascribed to the deposition of an external amorphous SiO_2 layer after the silylation treatment [20]. This is supported by TEM (Fig. 1) where, besides the typical lattice stripes of the zeolite, the presence of a surface amorphous layer of ca. 5 nm thickness was evidenced.

As for the mesoporous MFI-meso(22) sample, desilication of the starting MFI-c(22) zeolite lowered the bulk Si/Al ratio from 22 to 14 due to the selective removal of silicon from the zeolite framework by the basic NaOH and TBPOH reagents. Subsequent acid leaching with oxalic acid raised the bulk Si/Al from 14 to 22 and led to a surface Si/Al ratio of 31 due to the preferential elimination of Al species from the external surface and pore mouths of the zeolite. Finally, it is worth mentioning that the residual Na content determined by ICP-OES (not shown) was below 0.1 wt% for all samples.

Table 1
Physicochemical properties of H-ZSM-5 samples.

Sample	Si/Al at. ratio		Crystallite size (nm)	S_{BET} (m^2/g)	S_{ext}[b] (m^2/g)	V_{micro} (cm^3/g)
	Bulk	Near-surface[a]				
MFI-c (10)	10	11	~ 900[c]	368	13	0.17
MFI-c (16)	16	17	20–200[d]	372	40	0.16
MFI-c (22)	22	23	160[c]	374	61	0.15
MFI-c (31)	31	29	400–800	389	46	0.17
MFI-c (112)	112	106	400–2000[e]	369	20	0.16
MFI-sil (34)	34	41	400–800	330	24	0.15
MFI-nano (46)	46	47	20–40	450	170	0.13
MFI-meso (22)	22	31	50–200	569	316	0.12

[a] From XPS measurements.
[b] S_{ext} = external surface area.
[c] Taken from ref. [30].
[d] From ref. [38].
[e] From ref. [39].

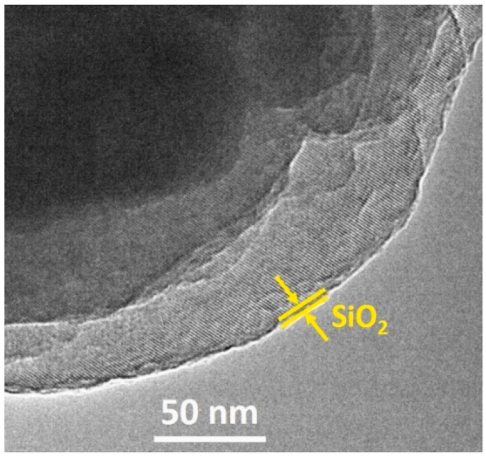

Fig. 1. TEM image of the silylated MFI-sil(34) sample. Coating by a 5 nm thick SiO_2 layer at the external crystallite surface is partially marked with yellow lines.

Regarding textural properties, the commercial samples displayed BET surface areas (362 – 389 m^2/g) and micropore volumes (0.15 – 0.17 cm^3/g) typical of H-ZSM-5 zeolite. The external surface area for these samples varied from 13 to 61 m^2/g showing, as expected, a general inverse relationship with their mean crystallite size. As observed in Table 1, the BET surface area and micropore volume of MFI-c(31) after the 3-cycle silylation treatment were reduced by ca. 15% and 12%, respectively, along with a decrease of about 50% in the external surface area (from 46 to 24 m^2/g). These changes in textural properties are closely related to the presence of an amorphous external SiO_2 layer, as discussed beforehand (Fig. 1). Moreover, analysis by (HR)FESEM (Fig. S3) revealed an analogous crystal morphology and crystallite size range (400 – 800 nm) for both the silylated and the parent MFI-c(31) samples (Table 1).

On the other hand, the MFI-nano(46) zeolite showed significantly higher BET and external surface areas (450 and 170 m^2/g, respectively) in comparison with the commercial samples, which is related to the nano-sized nature of the former exhibiting aggregates of very small crystallites sizing about 20 – 40 nm according to FESEM (Fig. S3) and TEM (Fig. 2) images. The micropore volume of this sample (0.13 cm^3/g) was somewhat lower than that of the commercial ones, which is most likely due to a relatively small loss of crystallinity during the air-calcination at 550 °C performed to remove the organic matter used in its synthesis.

As it can be seen in Table 1, the generation of mesoporosity in MFI-c (22) by desilication at the applied alkaline conditions (Section 2.1.2) produced a remarkable increase in the external surface area from 61 to 316 m^2/g and of the BET area from 389 to 569 m^2/g, accompanied by a certain loss of micropore volume (from 0.15 to 0.12 cm^3/g). The mesoporous sample did also display a reduced crystallite size of ca. 30 – 70 nm as estimated by FESEM (Fig. S3) in comparison to the parent MFI-c(22) sample (Table 1), which is related to the dissolution of silicon species from the solid. The presence of intra-crystal mesopores in MFI-meso(22), with diameters ranging about 5 – 10 nm, can be clearly visualized as light grey regions in the TEM image of Fig. 3.

The acid properties of the H-ZSM-5 samples were studied by FTIR spectroscopy of adsorbed pyridine (FTIR-Py) and, for selected samples, of 2,6-di-tert-butyl pyridine (FTIR-DTBPy).

The densities of Brønsted and Lewis acid sites determined by FTIR-Py at different pyridine desorption temperatures (250, 350, 400 °C) are presented in Table 2.

The results in Table 2 show that Brønsted acid sites are by far the most abundant in all the studied zeolites, with Brønsted-to-Lewis (B/L) acid site ratios of ca. 10 – 15 for the commercial samples and 3 – 6 for the silylated, nanocrystalline, and mesoporous ones. While Brønsted acid sites in aluminosilicate H-zeolites are known to be related to tetrahedrally coordinated Al species in the crystalline framework, the Lewis acidity is associated with the presence of Al species occupying extra-framework positions (generally referred to as EFAL). In close agreement with the FTIR-pyridine results, the ^{27}Al MAS NMR spectra of the hydrated zeolites (Fig. 4) indicate that Al is mostly in tetrahedral coordination (Al^{IV}), characterized by the signal at ca. 52 – 54 ppm, and therefore in the zeolite framework. Besides, the presence of a weak signal at ~ 0 ppm of Al in octahedral coordination (Al^{VI}) signs for the presence of EFAL species, albeit in a comparatively much lower concentration. In fact, the relative proportion of EFAL species estimated from the integrated areas of the Al^{IV} and Al^{VI} signals (values shown at the right side of the corresponding spectra in Fig. 4) was between 2% and 12% for all the zeolites except for the desilicated MFI-meso(22) one,

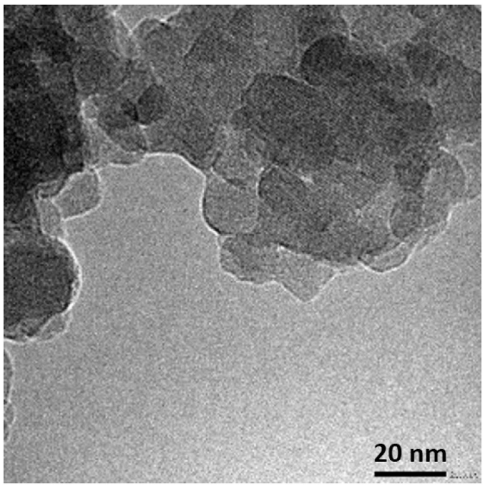

Fig. 2. Representative TEM image of the nanocrystalline MFI-nano(46) sample.

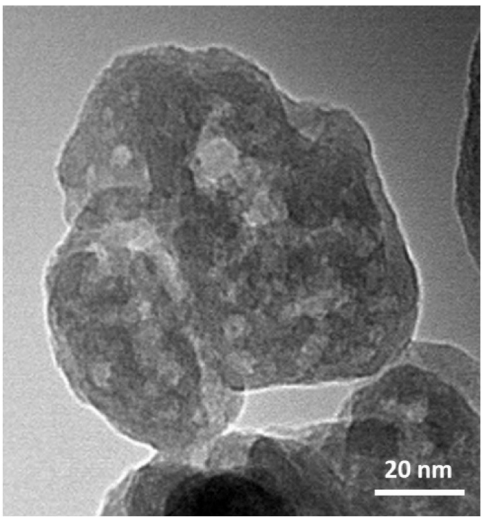

Fig. 3. Representative TEM image of the mesoporous MFI-meso(22) zeolite.

Table 2
Acidity of H-ZSM-5 samples determined by FTIR of adsorbed pyridine.

	Acidity (μmol/g)					
	Brønsted			Lewis		
Sample	250 °C	350 °C	400 °C	250 °C	350 °C	400 °C
MFI-c(10)	464	355	280	56	32	20
MFI-c(16)	387	323	304	34	32	27
MFI-c(22)	295	230	169	25	21	18
MFI-c(31)	206	146	97	14	10	8
MFI-c(112)	79	50	25	7	4	2
MFI-sil(34)	176	130	92	40	27	15
MFI-nano(46)	109	87	58	16	12	7
MFI-meso(22)	187	162	108	61	57	48

for which it amounted to 23% in line with its higher concentration of Lewis acid sites detected by FTIR-pyridine (Table 2). Since, as commented before, the Brønsted acid sites are related to tetrahedrally coordinated framework Al atoms, their density should be proportional to the amount of framework Al species. Indeed, as shown in Fig. S4, a reasonably good linear correlation ($R^2 = 0.94$) is obtained for the set of zeolites used here between the density of Brønsted acid sites measured at a pyridine desorption temperature of 250 °C and the concentration of framework Al calculated from the bulk Si/Al atomic ratio (ICP-OES) and the % of Al^{IV} species estimated by ^{27}Al MAS NMR.

3.2. CO_2 hydrogenation performance of K-Fe/γ-Al_2O_3+H-ZSM-5 catalysts

3.2.1. Activity and product selectivity

All catalysts displayed a quite stable performance with TOS in terms of CO_2 conversion and selectivity of CO and of total hydrocarbons (Fig. S5). This fact contrasts with that observed when a bulk Na-Fe_3O_4 catalyst instead of the supported K-Fe/γ-Al_2O_3 was used as iron component of tandem catalysts prepared also by the granule-mixing method with the same iron catalyst/zeolite mass ratio of 1:1. In that case, a gradual decline in CO_2 conversion accompanied by an increase in the selectivity of CO and CH_4 was noticed since the early reaction stages at equivalent reaction conditions (Fig. S6). These trends evidenced a progressive loss of iron promotion due to migration of the alkali from the iron component to the zeolite during reaction [40–42]. Therefore, the stable behaviour observed for the tandem catalysts based on K-Fe/γ-Al_2O_3 reported in this work suggests that alkali migration did not occur to a noticeable extent, at least within the range of TOS studied

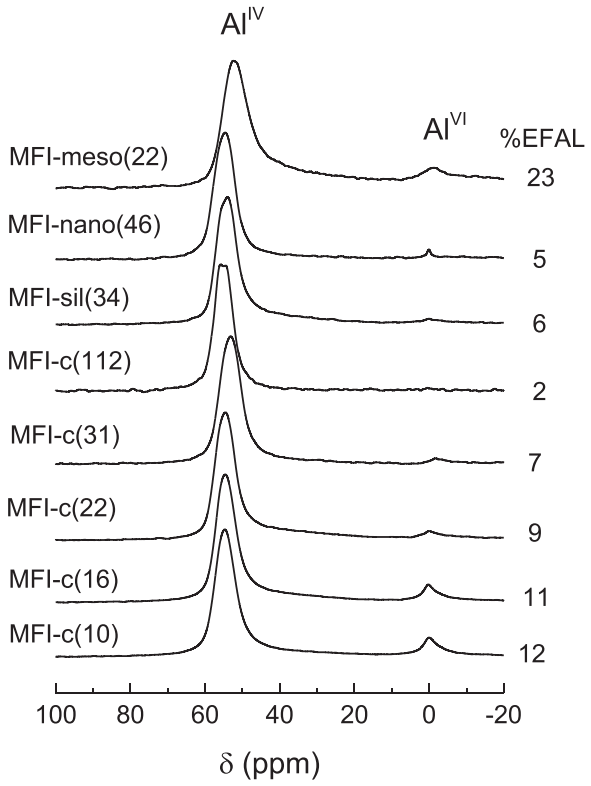

Fig. 4. ^{27}Al MAS NMR spectra of hydrated H-ZSM-5 samples. The percentage of Al species in octahedral (Al^{VI}) coordination for each zeolite is shown in the right-hand side of the corresponding spectrum.

here. The CO_2 conversion, CO selectivity, and overall hydrocarbons distribution obtained over the individual K-Fe/γ-Al_2O_3 catalyst and the tandem K-Fe/γ-Al_2O_3+H-ZSM-5 systems are summarized in Table 3.

As seen in the table, the conversion of CO_2 (X_{CO2}), the selectivity of CO (S_{CO}), and the selectivity of CH_4 in the hydrocarbons fraction ($S_{C1/HCs}$) remained almost unaltered upon the addition of zeolite to the Fe-based catalyst (X_{CO2} (%) = 52.5 ± 1.5, S_{CO} (%C) = 11.0 ± 1.0, $S_{C1/HCs}$ (%C) = 22.0 ± 2.0), indicating that these three catalytic parameters are mostly driven by the iron component of the multifunctional systems. Conversely, the presence of zeolite significantly changed the distribution of higher hydrocarbons, i.e. C_2-C_4 olefins and paraffins, and liquid (C_{5+}) hydrocarbons, in different extents depending on the specific H-ZSM-5 zeolite used. As a general trend, the tandem catalysts displayed lower selectivity of light olefins ($C_2^=$-$C_4^=$) and higher selectivity of C_{5+} hydrocarbons and light paraffins (C_2^0-C_4^0) in comparison to the bare Fe-based catalyst. As observed in the last column of Table 3, the enhanced selectivity of liquid hydrocarbons (C_{5+}) on the tandem catalysts is mostly related to the formation of aromatics which represented, for most of the zeolites, more than 50% of the C_{5+} fraction. Moreover, the hydrogen released in the aromatization reactions accounts for the saturation of olefins causing the observed decrease in the selectivity of $C_2^=$-$C_4^=$ and the concomitant increase in C_2^0-C_4^0 leading to a decreased olefin-to-paraffin ratio. In fact, the olefin-to-paraffin ratio for C_2-C_4 hydrocarbons exhibits a nearly linear decreasing trend with the concentration of aromatics in the C_{5+} fraction (Fig. S7). It is interesting to note that the catalyst containing the zeolite with the highest Si/Al ratio, MFI-c(112), exhibited a remarkable selectivity of valuable lower olefins ($C_2^=$-$C_4^=$) of 35.6%, exceeding that of the bare Fe catalyst (30.7%). The enhanced $C_2^=$-$C_4^=$ selectivity of this catalyst could be related to the acidity of this zeolite, too low to form aromatics in high amounts, as will be discussed in Section 3.2.2, but high enough to promote the cracking of heavier olefins produced over the Fe-based component. The lower selectivity of C_{5+} hydrocarbons of K-Fe/γ-Al_2O_3+MFI-c(112) (36.2%) with respect to the single iron catalyst (40.2%) provides support to the above explanation.

The most determinant zeolite properties for the formation of aromatics in the hydrogenation of CO_2 over this type of multifunctional catalysts will be discussed in the next section.

3.2.2. *Influence of zeolite properties on aromatics formation*

The olefin intermediates formed on the iron catalyst are transferred to the zeolite where the aromatization reactions take place via acid catalysis. Since Brønsted acid sites are generally the predominant type of acid sites in zeolites, as it is the case of the H-ZSM-5 samples studied here (Table 2), it seems reasonable that their concentration and/or strength should play an essential role in determining the aromatics selectivity. To this purpose, in Fig. 5 we have plotted the initial (at TOS ~ 1.5 h) selectivity to aromatics within hydrocarbons as a function of the density of Brønsted acid sites (BAS) of different acid strength as follows: BAS-w (weak BAS calculated as the difference between those retaining pyridine at 250 °C and at 350 °C), BAS-s+vs (strong+very strong BAS measured at a pyridine desorption temperature of 350 °C), and BAS-vs (very strong BAS retaining pyridine at 400 °C). As observed in Fig. 5, the aromatics

Table 3
Catalytic performance of K-Fe/γ-Al_2O_3+H-ZSM-5 catalysts for the hydrogenation of CO_2. Reaction conditions: 400 °C, 30 bar, H_2/CO_2 molar ratio of 3.1, space velocity (GHSV) of 4700 mL/($g_{Fe\text{-}cat}$·h). Data averaged for the last 3 h TOS.

Catalyst[a]	CO_2 conv. (%)	CO select. (%C)	Hydrocarbons distribution (% C)				Arom./C_{5+} (wt%)
			C_1	$C_2^=$-$C_4^=$	C_2^0-C_4^0	C_{5+}	
K-Fe/γ-Al_2O_3[b]	51.7	12.1	24.2	30.7	4.9	40.2	0.0
MFI-c(10)	51.2	11.7	20.6	5.0	25.2	49.2	66.4
MFI-c(16)	51.9	11.6	21.7	5.0	25.0	48.3	59.0
MFI-c(22)	52.9	10.5	20.5	7.5	18.7	53.3	57.1
MFI-c(31)	53.4	11.0	20.2	8.4	21.0	50.4	53.5
MFI-c(112)	54.0	10.4	21.9	35.6	6.3	36.2	16.1
MFI-sil(34)	52.6	10.3	21.0	12.4	17.8	48.8	52.3
MFI-nano (46)	51.1	11.2	22.0	25.6	8.5	43.9	30.2
MFI-meso (22)	53.4	10.1	21.1	12.1	17.2	49.6	49.6

[a] For simplicity, only the name of the zeolite is given.
[b] The Fe-based catalyst produced, besides CO and hydrocarbons, oxygenates (primarily C_1-C_3 alcohols) with a total selectivity of 3.8%C.

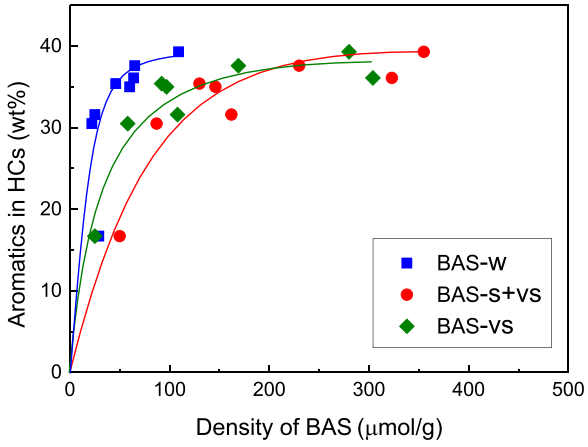

Fig. 5. Initial (TOS = 1.5 h) selectivity of aromatics in hydrocarbons as a function of the density of weak (BAS-w), strong+very strong (s+vs), and very strong (BAS-vs) Brønsted acid sites in H-ZSM-5 zeolite (see text). Reaction conditions: 400 °C, 30 bar, H_2/CO_2 molar ratio of 3.1, space velocity (GHSV) of 4700 mL/($g_{Fe\text{-}cat}$·h).

selectivity showed an initial rapid rise with the concentration of Brønsted acid sites followed by a smoother increase above a certain site density, in close agreement with the trend observed by Wei et al. [21] in the hydrogenation of CO_2 to aromatics over composite Na-Fe_3O_4+H-ZSM-5 catalysts. The similar dependence of the aromatics selectivity with the amount of Brønsted acid sites of different acid strength (Fig. 5) suggests that all Brønsted acid sites titrated by pyridine at 250 °C should be involved in the aromatization of olefin intermediates at the relatively high reaction temperature (400 °C) employed in our study. Nonetheless, we observed a certain positive correlation between the aromatics selectivity and the fraction of strong Brønsted acid sites, expressed as the ratio of the amount of acid sites retaining pyridine at 400 °C to those at 250 °C (BAS_{400}/BAS_{250} ratio) (Fig. S8), pointing towards a more favourable formation of aromatics on the sites with higher acid strength.

On the other hand, the fact that a minimum density of Brønsted acid sites is required to achieve high selectivity to aromatics could be linked with the presence of the so-called Al pairs, more abundant in the samples with higher framework Al content, on which aromatics were proposed to be preferentially formed from either olefins [43] or methanol [44]. Therefore, from the results discussed beforehand we may conclude that, under our reaction conditions, the zeolite Brønsted acidity is a more relevant parameter determining the aromatics selectivity than either crystallite size or mesoporosity.

In a previous study, the formation rate of aromatics from syngas over a tandem Na-Fe-ZrO_2/H-ZSM-5 catalyst was found proportional to the number of Lewis acid sites that would be active for olefin aromatization through the dehydroaromatization mechanism [9]. However, in the present work we didn't find a clear relationship between the selectivity of aromatics and the concentration of Lewis acid sites (at any pyridine desorption temperature) or the Lewis-to-Brønsted acid site (LAS/BAS) ratio (Fig. S9). Thus, our results point to a minor role (if any) of Lewis-type acid sites in the aromatization reactions, at least in our conditions. In the same line, several other studies also concluded that Brønsted acid sites played a more relevant role than Lewis acid sites in the aromatization of olefins over H-ZSM-5 [14,43].

In spite of the stable performance in terms of CO_2 conversion and CO and hydrocarbons selectivity observed for the K-Fe/γ-Al_2O_3+H-ZSM-5 catalysts (Fig. S5), a progressive decline of aromatics selectivity with TOS was noticed (Fig. 6). Such deactivation behaviour is common during aromatization reactions over H-ZSM-5 and is generally attributed to deposition of coke on the zeolite acid sites [4,5,14,45].

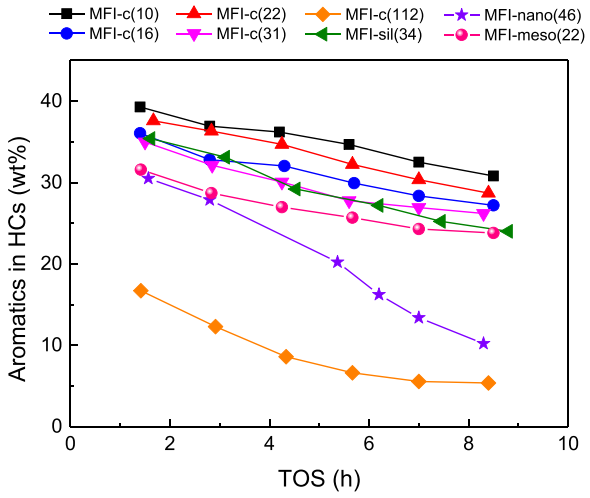

Fig. 6. Variation of the selectivity of aromatics in the hydrocarbons fraction as a function of TOS for the tandem K-Fe/γ-Al_2O_3+H-ZSM-5 catalysts. Reaction conditions as in Fig. 5. For the sake of clarity, only the name of the zeolite is shown in the legend.

As inferred from Fig. 6, the relative loss of aromatics selectivity in the range of TOS of ca. 1.5 – 8.5 h is remarkably higher (66 – 68%) for the catalysts comprising the MFI-c(112) and the nanocrystalline MFI-nano (46) samples in comparison with the rest of catalysts, which present relative losses of 20 – 30%. Considering that a minimum amount of Brønsted acid sites is required to promote the formation of aromatics (Fig. 5), it seems reasonable to speculate that deposition of coke should have a more drastic effect on aromatics selectivity in the MFI-c(112) and MFI-nano(46) zeolites possessing the lowest amount of Brønsted acid sites (Table 2) and, expectedly, of Al pairs that, as discussed before, are believed to play a relevant role in the aromatics formation. In the case of the MFI-nano(46) zeolite comprising small crystallites sizing only 20 – 40 nm (Fig. 2) and thus high external surface area (Table 1), a higher contribution of side reactions occurring on the unconstrained external acid sites leading to coke would also probably contribute to its relatively high loss of aromatization activity [24].

3.2.3. *Formation of BTEX aromatics*

Among the aromatic hydrocarbons, the fraction constituted by benzene, toluene, ethylbenzene, and xylenes (BTEX) is the most demanded and thus of higher economic value. The selectivity of BTEX in the total aromatics fraction obtained in the present work on the tandem K-Fe/γ-Al_2O_3+H-ZSM-5 catalysts, averaged for TOS = 5.5 – 8.5 h, is shown in Fig. 7. As observed in the figure, the catalyst that exhibited the highest BTEX selectivity (74.6 wt% of total aromatics) was that based on the silylated MFI-sil(34) zeolite, followed by that containing the commercial MFI-c(10) zeolite with the lowest Si/Al ratio (70.2 wt%). On the opposite side, the nano-sized MFI-nano(46) zeolite showed the lowest BTEX selectivity (35.7 wt%) while that of the desilicated MFI-meso(22) sample was also comparatively low (46.2 wt%).

For catalysts based on the (untreated) commercial zeolites, the BTEX selectivity exhibited a general increasing trend from 42.3 to 70.2 wt% with increasing the total amount as well as the fraction of strong Brønsted acid sites (Fig. S10), suggesting that, similar to what was concluded for total aromatics (Fig. 5), both parameters would positively affect the BTEX selectivity. However, a clear correlation between BTEX selectivity and Brønsted acidity, both in terms of density and strength, could not be evidenced when considering the whole set of zeolites (Fig. S11). Indeed, as highlighted in Fig. S11, the catalysts based on MFI-c(31), MFI-meso(22), and MFI-sil(34) having comparable density (176 – 206 μmol/g) and strength (BAS_{400}/BAS_{250} ratio = 0.47 – 0.58) of Brønsted acid sites displayed extremely different BTEX selectivity values (46.2 – 74.6 wt%). At this point, it should be considered that the formation of light BTEX aromatics preferentially occurs on the acid sites

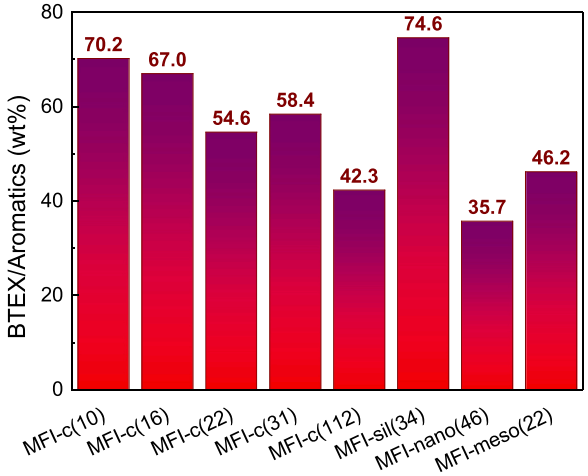

Fig. 7. BTEX selectivity in total aromatics for the tandem K-Fe/γ-Al_2O_3+H-ZSM-5 catalysts. Reaction conditions as in Fig. 5. For the sake of clarity, only the name of the zeolite is displayed in the x-axe.

located within the zeolite micropores while those at the external surface are less selective to this fraction by promoting the formation of heavier aromatics through secondary reactions of the lighter ones [46].

In order to assess the influence of the external Brønsted acid sites on BTEX selectivity without being masked by the possible contribution of the total Brønsted acidity, as discussed beforehand, we measured the FTIR spectra of adsorbed 2,6-di-tert-butyl pyridine (FTIR-DTBPy) for the three zeolites mentioned before displaying alike total Brønsted acidity albeit quite distinct BTEX selectivity. The corresponding spectra in the region where the IR band at 1615 cm^{-1} attributed to the ring vibration of protonated 2,6-DTBPy (2,6-DTBPyH$^+$) appears [33] are presented in Fig. 8. As observed, the intensity of the band at 1615 cm^{-1} for the silylated sample (I_{1615} = 0.008 a.u.) was reduced by ca. 90% with respect to its original MFI-c(31) counterpart (I_{1615} = 0.074 a.u.), signing for a concomitant decrease in the concentration of external Brønsted acid sites. On the contrary, the intensity of this band in the desilicated MFI-meso(22) (I_{1615} = 0.539 a.u.) sample was about 7 and 67 times higher than in MFI-c(31) and MFI-sil(34), respectively. This implies an equivalent increase in the amount of accessible external Brønsted acid sites in the former as a consequence of the abundant mesopores generated in the desilication process (Table 1, Fig. 3).

Looking back to the results in Fig. 7, an inverse correlation between the BTEX selectivity and the external Brønsted acidity becomes evident for these three zeolites possessing comparable total Brønsted acidity, with the catalyst based on the surface-passivated MFI-sil(34) zeolite exhibiting the maximum BTEX selectivity of ca. 75% in the aromatics fraction. This value is among the highest reported in CO_2 hydrogenation through the FT-mediated route over composite Fe-based+H-ZSM-5 catalysts [21]. We can thus conclude that, although both the total density of Brønsted acid sites and the accessible ones on the external surface were shown to affect the formation of BTEX at the conditions studied here, the latter parameter was undoubtedly the most determinant to achieving high BTEX selectivity.

4. Conclusions

In this study, a set of eight commercial and home-prepared H-ZSM-5 samples with varying acidity, crystallite size, and mesoporosity was used to assess the most relevant zeolite parameters determining the selectivity of aromatics as well as of the most valuable BTEX fraction in the hydrogenation of CO_2 over tandem K-Fe/γ-Al_2O_3+H-ZSM-5 catalysts. The selectivity of aromatics in hydrocarbons was found to rapidly rise with the density of Brønsted acid sites (BAS) of H-ZSM-5 zeolite up to a certain value above which it increased smoothly. Even though our results suggested that, at the relatively high reaction temperature used in this study (400 °C), all BAS titrated by pyridine at 250 °C participated in the aromatization of the olefin intermediates, the formation of aromatics appeared to be favoured on the acid sites of higher strength. Accordingly, a maximum initial (at ca. 1.5 h TOS) aromatics selectivity of about 79% in C_{5+} (~ 40% in total hydrocarbons) was reached for the zeolite with SiAl = 10 possessing the highest density of total BAS and a high fraction of strong-to-total BAS. All catalysts displayed a gradual loss of aromatics selectivity with TOS, much less pronounced (20 – 25% relative to the initial values after ca. 8.5 on stream) for those containing zeolites with high density of BAS. On the other hand, we didn't find any clear correlation between the aromatics selectivity and the amount of Lewis acid sites, signing for a minor role (if any) of this type of acid sites in the olefin aromatization reactions. Moreover, although a general positive influence of the concentration and strength of BAS on the selectivity of BTEX aromatics was inferred in this work, the external Brønsted acidity was found the most relevant zeolite property for the selective formation of BTEX. Indeed, for zeolites MFI-c(31), MFI-sil(34), and MFI-meso(22) possessing a comparable density and strength of BAS, an inverse correlation between the BTEX selectivity and the external Brønsted acidity, qualitatively assessed by FTIR-DTBPy, was clearly observed. Particularly, the MFI-sil(34) sample that was submitted to a surface-passivation treatment by silylation achieved a remarkably high BTEX selectivity (in aromatics) of 75%, which stands out among the highest values reported in the hydrogenation of CO_2 over Fe-based+H-ZSM-5 catalysts following the FT-mediated route.

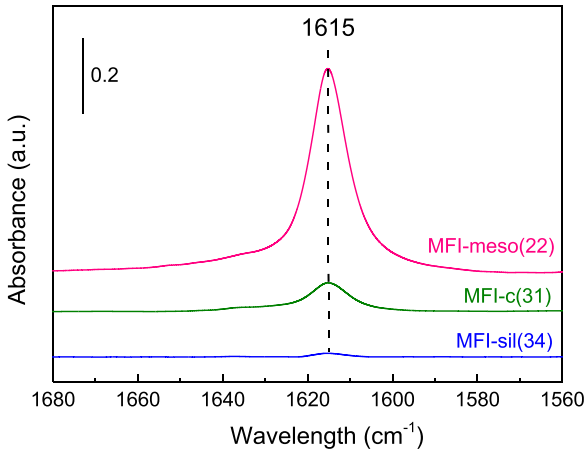

Fig. 8. FTIR-DTBPy spectra of MFI-c(31), MFI-sil(34), and MFI-meso(22) zeolites. The spectra were normalized to sample weight.

CRediT authorship contribution statement

Raúl Murciano: Investigation, Resources. **José M. Serra:** Conceptualization, Funding acquisition. **Agustín Martínez:** Conceptualization, Supervision, Writing – original draft, Writing – review & editing.

Declaration of Competing Interest

The authors declare that they have no known competing financial interests or personal relationships that could have appeared to influence the work reported in this paper.

Data Availability

No data was used for the research described in the article.

Acknowledgments

This work has received European Union's Horizon 2020 Research and Innovation funding under grant agreement No 838077 (eCOCO$_2$ project). Funding by the Generalitat Valenciana through the Prometeo CIPROM/2022/10 project is also acknowledged. This study was supported by MICIN with funding from European NextGenerationEU (PRTR-C17. I1) within the Green Hydrogen and Energy Program-CSIC and CSIC Interdisciplinary Thematic Platform (PTI+) Transición Energética Sostenible+ (PTI-TRANSENER+). We are grateful to Dr. S. Escorihuela, Dr. M. Navarro, and Dr. J.A. Vidal-Moya for their assistance in part of the experimental work. The authors are also thankful to the Microscopy Service of the Universitat Politècnica de València (UPV).

Appendix A. Supporting information

Supplementary data associated with this article can be found in the online version at doi:10.1016/j.cattod.2023.114404.

References

[1] W. Zhou, K. Cheng, J. Kang, C. Zhou, V. Subramanian, Q. Zhang, Y. Wang, New horizon in C1 chemistry: breaking the selectivity limitation in transformation of syngas and hydrogenation of CO_2 into hydrocarbon chemicals and fuels, Chem. Soc. Rev. 48 (2019) 3193–3228, https://doi.org/10.1039/c8cs00502h.

[2] J. Artz, T.E. Müller, K. Thenert, J. Kleinekorte, R. Meys, A. Sternberg, A. Bardow, W. Leitner, Sustainable Conversion of carbon dioxide: an integrated review of catalysis and life cycle assessment, Chem. Rev. 118 (2018) 434–504, https://doi.org/10.1021/acs.chemrev.7b00435.

[3] Page website: https://ecoco2.eu./.

[4] Y. Xu, C. Shi, B. Liu, T. Wang, J. Zheng, W. Li, D. Liu, X. Liu, Selective production of aromatics from CO 2, Catal. Sci. Technol. 9 (2019) 593–610, https://doi.org/10.1039/c8cy02024h.

[5] I. Nezam, W. Zhou, G.S. Gusmão, M.J. Realff, Y. Wang, A.J. Medford, C.W. Jones, Direct aromatization of CO2via combined CO2hydrogenation and zeolite-based acid catalysis, J. CO_2 Util. 45 (2021), https://doi.org/10.1016/j.jcou.2020.101405.

[6] X. Pan, F. Jiao, D. Miao, X. Bao, Oxide-zeolite-based composite catalyst concept that enables syngas chemistry beyond fischer-tropsch synthesis, Chem. Rev. 121 (2021) 6588–6609, https://doi.org/10.1021/acs.chemrev.0c01012.

[7] Y. Wang, L. Tan, M. Tan, P. Zhang, Y. Fang, Y. Yoneyama, G. Yang, N. Tsubaki, Rationally designing bifunctional catalysts as an efficient strategy to boost CO 2 hydrogenation producing value-added aromatics, ACS Catal. 9 (2019) 895–901, https://doi.org/10.1021/acscatal.8b01344.

[8] Y. Song, X. Zhu, L. Xu, Study on the process of transformation of olefin into aromatics over HZSM-5, Catal. Commun. 7 (2006) 218–223, https://doi.org/10.1016/j.catcom.2005.11.007.

[9] X. Yang, R. Wang, J. Yang, W. Qian, Y. Zhang, X. Li, Y. Huang, T. Zhang, D. Chen, Exploring the reaction paths in the consecutive Fe-based FT catalyst-zeolite process for syngas conversion, ACS Catal. 10 (2020) 3797–3806, https://doi.org/10.1021/acscatal.9b05449.

[10] Y. Ni, Z. Chen, Y. Fu, Y. Liu, W. Zhu, Z. Liu, Selective conversion of CO_2 and H2 into aromatics, Nat. Commun. 9 (2018) 1–7, https://doi.org/10.1038/s41467-018-05880-4.

[11] Z. Li, J. Wang, Y. Qu, H. Liu, C. Tang, S. Miao, Z. Feng, H. An, C. Li, Highly selective conversion of carbon dioxide to lower olefins, ACS Catal. 7 (2017) 8544–8548, https://doi.org/10.1021/acscatal.7b03251.

[12] H. Tian, J. Jiao, F. Zha, X. Guo, X. Tang, Y. Chang, H. Chen, Hydrogenation of CO2into aromatics over ZnZrO-Zn/HZSM-5 composite catalysts derived from ZIF-8, Catal. Sci. Technol. 12 (2022) 799–811, https://doi.org/10.1039/d1cy01570b.

[13] G. Song, Q. Jiang, Y. Zhai, D. Liu, Rationally designing NaFeMn/core–shell HZSM-5@Si bifunctional catalyst for selective synthesis of para-Xylene from CO_2 hydrogenation, Chem. Eng. Sci. 280 (2023), 119037, https://doi.org/10.1016/j.ces.2023.119037.

[14] C. Zhang, K. Hu, X. Chen, L. Xu, C. Deng, Q. Wang, R. Gao, K.W. Jun, S.K. Kim, T. Zhao, H. Wan, G. Guan, Direct hydrogenation of CO_2 into valuable aromatics over K/Fe-Cu-Al @HZSM-5 tandem catalysts: effects of zeolite surface acidity on aromatics formation, Fuel Process. Technol. 248 (2023), 107824, https://doi.org/10.1016/j.fuproc.2023.107824.

[15] J. Liang, L. Guo, W. Gao, C. Wang, X. Guo, Y. He, G. Yang, N. Tsubaki, Direct conversion of CO2to aromatics over K-Zn-Fe/ZSM-5 catalysts via a fischer-tropsch synthesis pathway, Ind. Eng. Chem. Res. 61 (2022) 10336–10346, https://doi.org/10.1021/acs.iecr.1c05061.

[16] P. Lu, J. Liang, K. Wang, B. Liu, T. Atchimarungsri, Y. Wang, X. Zhang, J. Tian, Y. Jiang, Z. Liu, P. Reubroycharoen, T. Zhao, J. Zhang, X. Gao, Boosting liquid hydrocarbon synthesis from CO2 hydrogenation via tailoring acid properties of HZSM-5 zeolite, Ind. Eng. Chem. Res. 61 (2022) 16393–16401, https://doi.org/10.1021/acs.iecr.2c03132.

[17] C. Dai, X. Zhao, B. Hu, J. Zhang, Q. Hao, H. Chen, X. Guo, X. Ma, Hydrogenation of CO2to aromatics over Fe-K/Alkaline Al2O3and P/ZSM-5 tandem catalysts, Ind. Eng. Chem. Res. 59 (2020) 19194–19202, https://doi.org/10.1021/acs.iecr.0c03598.

[18] Y. Wang, W. Gao, K. Wang, X. Gao, B. Zhang, H. Zhao, Q. Ma, P. Zhang, G. Yang, M. Wu, N. Tsubaki, Boosting the synthesis of value-added aromatics directly from syngasviaa Cr2O3and Ga doped zeolite capsule catalyst, Chem. Sci. 12 (2021) 7786–7792, https://doi.org/10.1039/d1sc01859k.

[19] C. Liu, J. Su, S. Liu, H. Zhou, X. Yuan, Y. Ye, Y. Wang, W. Jiao, L. Zhang, Y. Lu, Y. Wang, H. He, Z. Xie, Insights into the key factor of zeolite morphology on the selective conversion of syngas to light aromatics over a Cr2O3/ZSM-5 catalyst, ACS Catal. 10 (2020) 15227–15237, https://doi.org/10.1021/acscatal.0c03658.

[20] Y. Fang, Z. Huang, S. Wang, H. Sheng, W. Hua, Y. Yue, W. Shen, H. Xu, Enhancing BTX selectivity of the syngas to aromatics reaction through silylation of CTAB pretreated ZSM-5, Catal. Sci. Technol. 11 (2021) 4944–4952, https://doi.org/10.1039/d1cy00781e.

[21] J. Wei, R. Yao, Q. Ge, D. Xu, C. Fang, J. Zhang, H. Xu, J. Sun, Precisely regulating Brønsted acid sites to promote the synthesis of light aromatics via CO_2 hydrogenation, Appl. Catal. B Environ. 283 (2021), 119648, https://doi.org/10.1016/j.apcatb.2020.119648.

[22] D. Miao, Y. Ding, T. Yu, J. Li, X. Pan, X. Bao, Selective synthesis of benzene, toluene, and xylenes from syngas, ACS Catal. 10 (2020) 7389–7397, https://doi.org/10.1021/acscatal.9b05200.

[23] W. Gao, L. Guo, Q. Wu, C. Wang, X. Guo, Y. He, P. Zhang, G. Yang, G. Liu, J. Wu, N. Tsubaki, Capsule-like zeolite catalyst fabricated by solvent-free strategy for para-Xylene formation from CO_2 hydrogenation, Appl. Catal. B Environ. 303 (2022), 120906, https://doi.org/10.1016/j.apcatb.2021.120906.

[24] Z. Ma, X. Wang, X. Ma, M. Tan, G. Yang, Y. Tan, Catalytic roles of acid property in different morphologies of H-ZSM-5 zeolites for syngas-to-aromatics conversion over ZnCrOx/H-ZSM-5 catalysts, Microporous Mesoporous Mater. 349 (2023), 112420, https://doi.org/10.1016/j.micromeso.2022.112420.

[25] J. Yang, K. Gong, D. Miao, F. Jiao, X. Pan, X. Meng, F. Xiao, X. Bao, Enhanced aromatic selectivity by the sheet-like ZSM-5 in syngas conversion, J. Energy Chem. 35 (2019) 44–48, https://doi.org/10.1016/j.jechem.2018.10.008.

[26] Y. Wang, S. Kazumi, W. Gao, X. Gao, H. Li, X. Guo, Y. Yoneyama, G. Yang, N. Tsubaki, Direct conversion of CO_2 to aromatics with high yield via a modified Fischer-Tropsch synthesis pathway, Appl. Catal. B Environ. 269 (2020), 118792, https://doi.org/10.1016/j.apcatb.2020.118792.

[27] S. Zheng, H.R. Heydenrych, A. Jentys, J.A. Lercher, Influence of surface modification on the acid site distribution of HZSM-5, J. Phys. Chem. B 106 (2002) 9552–9558, https://doi.org/10.1021/jp014091d.

[28] R.W. Weber, K.P. Möller, C.T. O'Connor, The chemical vapour and liquid deposition of tetraethoxysilane on ZSM-5, mordenite and beta, Microporous Mesoporous Mater. 35– 36 (2000) 533–543, https://doi.org/10.1016/S1387-1811(99)00248-6.

[29] S. Al-Khattaf, S.A. Ali, A.M. Aitani, N. Žilková, D. Kubička, J. Čejka, Recent advances in reactions of alkylbenzenes over novel zeolites: The effects of zeolite structure and morphology, Catal. Rev. - Sci. Eng. 56 (2014) 333–402, https://doi.org/10.1080/01614940.2014.946846.

[30] A. Corma, C. Martínez, E. Doskocil, Designing MFI-based catalysts with improved catalyst life for C 3 = and C 5 = oligomerization to high-quality liquid fuels, J. Catal. 300 (2013) 183–196, https://doi.org/10.1016/j.jcat.2012.12.029.

[31] C.A. Emeis, Determination of integrated molar extinction coefficients for infrared absorption bands of pyridine adsorbed on solid acid catalysts, J. Catal. 141 (1993) 347–354, https://doi.org/10.1006/jcat.1993.1145.

[32] A. Corma, V. Fornés, L. Forni, F. Márquez, J. Martínez-Triguero, D. Moscotti, 2,6-Di-tert-butyl-pyridine as a probe molecule to measure external acidity of zeolites, J. Catal. 179 (1998) 451–458, https://doi.org/10.1006/jcat.1998.2233.

[33] K. Góra-Marek, K. Tarach, M. Choi, 2,6-Di-tert-butylpyridine sorption approach to quantify the external acidity in hierarchical zeolites, J. Phys. Chem. C 118 (2014) 12266–12274, https://doi.org/10.1021/jp501928k.

[34] A. Martínez, C. López, F. Márquez, I. Díaz, Fischer-Tropsch synthesis of hydrocarbons over mesoporous Co/SBA-15 catalysts: the influence of metal loading, cobalt precursor, and promoters, J. Catal. 220 (2003) 486–499, https://doi.org/10.1016/S0021-9517(03)00289-6.

[35] K. Opeyemi Otun, Y. Yao, X. Liu, D. Hildebrandt, Synthesis, structure, and performance of carbide phases in Fischer-Tropsch synthesis: a critical review, Fuel 296 (2021), 120689, https://doi.org/10.1016/j.fuel.2021.120689.

[36] T.A. Wezendonk, X. Sun, A.I. Dugulan, A.J.F. van Hoof, E.J.M. Hensen, F. Kapteijn, J. Gascon, Controlled formation of iron carbides and their performance in Fischer-Tropsch synthesis, J. Catal. 362 (2018) 106–117, https://doi.org/10.1016/j.jcat.2018.03.034.

[37] S. Janbroers, J.N. Louwen, H.W. Zandbergen, P.J. Kooyman, Insights into the nature of iron-based Fischer-Tropsch catalysts from quasi in situ TEM-EELS and XRD, J. Catal. 268 (2009) 235–242, https://doi.org/10.1016/j.jcat.2009.09.021.

[38] J. Oenema, J. Harmel, R.P. Vélez, M.J. Meijerink, W. Eijsvogel, A. Poursaeidesfahani, T.J.H. Vlugt, J. Zečević, K.P. De Jong, Influence of Nanoscale Intimacy and Zeolite Micropore Size on the Performance of Bifunctional Catalysts for n-Heptane Hydroisomerization, ACS Catal. 10 (2020) 14245–14257, https://doi.org/10.1021/acscatal.0c03138.

[39] J. Van Aelst, A. Philippaerts, E. Bartholomeeusen, E. Fayad, F. Thibault-Starzyk, J. Lu, D. Schryvers, R. Ooms, D. Verboekend, P. Jacobs, B. Sels, Towards biolubricant compatible vegetable oils by pore mouth hydrogenation with shape-selective Pt/ZSM-5 catalysts, Catal. Sci. Technol. 6 (2016) 2820–2828, https://doi.org/10.1039/c6cy00498a.

[40] F.G. Botes, W. Böhringer, The addition of HZSM-5 to the Fischer-Tropsch process for improved gasoline production, Appl. Catal. A Gen. 267 (2004) 217–225, https://doi.org/10.1016/j.apcata.2004.03.006.

[41] J.L. Weber, N.A. Krans, J.P. Hofmann, E.J.M. Hensen, J. Zecevic, P.E. de Jongh, K. P. de Jong, Effect of proximity and support materials on deactivation of bifunctional catalysts for the conversion of syngas to olefins and aromatics, Catal. Today 342 (2020) 161–166, https://doi.org/10.1016/j.cattod.2019.02.002.

[42] D. Xu, H. Fan, K. Liu, G. Hou, C. Qin, Y. Xu, R. Li, J. Wang, M. Ding, Impacts of interaction between active components on catalyst deactivation over KFe/ZSM-5 bifunctional catalyst, ACS Sustain. Chem. Eng. 11 (2023) 10441–10452, https://doi.org/10.1021/acssuschemeng.3c01826.

[43] L. Zhang, H. Zhang, Z. Chen, Q. Ning, S. Liu, J. Ren, X. Wen, Y.W. Li, Insight into the impact of Al distribution on the catalytic performance of 1-octene aromatization over ZSM-5 zeolite, Catal. Sci. Technol. 9 (2019) 7034–7044, https://doi.org/10.1039/c9cy01672d.

[44] Y. Zhou, H. Liu, X. Rao, Y. Yue, H. Zhu, X. Bao, Controlled synthesis of ZSM-5 zeolite with an unusual Al distribution in framework from natural aluminosilicate mineral, Microporous Mesoporous Mater. 305 (2020), 110357, https://doi.org/10.1016/j.micromeso.2020.110357.

[45] J.L. Weber, D. Martínez del Monte, R. Beerthuis, J. Dufour, C. Martos, K.P. de Jong, P.E. de Jongh, Conversion of synthesis gas to aromatics at medium temperature with a fischer tropsch and ZSM-5 dual catalyst bed, Catal. Today 369 (2021) 175–183, https://doi.org/10.1016/j.cattod.2020.05.016.

[46] N.J. Azhari, N. Nurdini, S. Mardiana, T. Ilmi, A.T.N. Fajar, I.G.B.N. Makertihartha, G.T.M. Subagjo, Kadja, Zeolite-based catalyst for direct conversion of CO_2 to C2+ hydrocarbon: a review, J. CO_2 Util. 59 (2022), 101969, https://doi.org/10.1016/j.jcou.2022.101969.